

Dynamic subauroral ionospheric electric fields observed by the Falkland Islands radar during the course of a geomagnetic storm

A. Grocott,¹ S. E. Milan,¹ J. B. H. Baker,² M. P. Freeman,³ M. Lester,¹ and T. K. Yeoman¹

Received 18 April 2011; revised 22 August 2011; accepted 23 August 2011; published 4 November 2011.

[1] We present an analysis of ionospheric electric field data observed during a geomagnetic storm by the recently deployed HF radar located on the Falkland Islands. On 3 August 2010 at ~1800 UT evidence of the onset of a geomagnetic storm was observed in ground magnetometer data in the form of a decrease in the Sym-H index of ~100 nT. The main phase of the storm was observed to last ~24 hours before a gradual recovery lasting ~3 days. On 4 August, during the peak magnetic disturbance of the storm, a high velocity ($>1000 \text{ m s}^{-1}$) channel of ionospheric plasma flow, which we interpret as a subauroral ion drift (SAID), located between 53° and 58° magnetic south and lasting ~6.5 hours, was observed by the Falkland Islands radar in the pre-midnight sector. Coincident flow data from the DMSP satellites and the magnetically near-conjugate northern hemisphere Blackstone HF radar reveal that the SAID was embedded within the broader subauroral polarization streams (SAPS). DMSP particle data indicate that the SAID location closely followed the equatorward edge of the auroral electron precipitation boundary, while remaining generally poleward of the equatorward boundary of the ion precipitation. The latitude of the SAID varied throughout the interval on similar timescales to variations in the interplanetary magnetic field and auroral activity, while variations in its velocity were more closely related to ring current dynamics. These results are consistent with SAID electric fields being generated by localized charge separation in the partial ring current, but suggest that their location is more strongly governed by solar wind driving and associated large-scale magnetospheric dynamics.

Citation: Grocott, A., S. E. Milan, J. B. H. Baker, M. P. Freeman, M. Lester, and T. K. Yeoman (2011), Dynamic subauroral ionospheric electric fields observed by the Falkland Islands radar during the course of a geomagnetic storm, *J. Geophys. Res.*, **116**, A11202, doi:10.1029/2011JA016763.

1. Introduction

[2] Ionospheric electric fields play a vital role in controlling the dynamics of the upper atmosphere. They are directly associated with convection of ionospheric plasma while at the same time providing a major source of heat and momentum to the neutral atmosphere via joule heating. They are also hugely important in diagnosing the solar-terrestrial interaction owing to the coupled nature of the solar wind-magnetosphere-ionosphere system. Measurements of the ionospheric electric fields can, for example, inform us about the spatiotemporal evolution of large-scale magnetospheric structures of which in-situ satellite observations can only make point measurements. In the dayside

ionosphere and polar cap the nature of the electric field is governed largely by the direct interaction of the magnetosphere with the solar wind. For example, when reconnection occurs between the interplanetary and terrestrial magnetic fields convection is excited in the magnetosphere producing a significant enhancement in the ionospheric electric field [e.g., Etemadi *et al.*, 1988; Todd *et al.*, 1988; Ruohoniemi *et al.*, 1993; Provan *et al.*, 2005]. On the nightside, internal magnetospheric processes, such as substorms, deposit huge amounts of energy and momentum into the ionosphere severely affecting its composition and electrodynamics [e.g., Akasofu, 1964; Kirkwood *et al.*, 1988; Lui, 1996; Elphinstone *et al.*, 1996]. One such effect is to enhance the electric field in a similar fashion to the solar wind-magnetosphere interaction at the dayside [e.g., Grocott *et al.*, 2002], yet at the same time the electric field can suffer localized suppressions and major reorientations due to enhanced conductivities and field-aligned currents [Morelli *et al.*, 1995; Yeoman *et al.*, 2000; Grocott *et al.*, 2009].

[3] One aspect of the complexity of substorm electrodynamics concerns the coupling of auroral zone electric fields, associated with convection and the Harang discontinuity

¹Department of Physics and Astronomy, University of Leicester, Leicester, UK.

²Bradley Department of Electrical and Computer Engineering, Virginia Polytechnic Institute and State University, Blacksburg, Virginia, USA.

³British Antarctic Survey, Natural Environment Research Council, Cambridge, UK.

[e.g., *Grocott et al.*, 2006; *Zou et al.*, 2009a, 2009b; *Grocott et al.*, 2010], to subauroral electric fields, discussed below. A variety of observations of subauroral electric fields have been reported, identified by a variety of instrumentation during various levels of geomagnetic activity and referred to by an abundant array of names including polarization jets (PJ) [Galperin et al., 1973], subauroral ion drifts (SAID) [Spiro et al., 1979], substorm associated radar auroral surges (SARAS) [Freeman et al., 1992], subauroral electric fields (SAEF) [Karlsson et al., 1998], subauroral polarization streams (SAPS) [Foster and Burke, 2002] and auroral-westward flow channels (AWFC) [Parkinson et al., 2003]. In general, these phenomena are observed in the pre-midnight ionosphere although the term SAPS is used to encompass the full range of electric fields observed in the subauroral region including the broad ($\sim 5^\circ$), weak ($\sim 100 \text{ m s}^{-1}$) background flows which persist beyond midnight into the pre-dawn sector. SAID, on the other hand, are fast ($1\text{--}4 \text{ km s}^{-1}$), latitudinally narrow ($\sim 1^\circ\text{--}2^\circ$) regions of rapid westward ion drift explicitly associated with substorm electrodynamics. Located in the evening sector on the equatorward edge of the diffuse aurora, SAID are believed to be generated by polarization electric fields, resulting from the penetration of partial ring current ions to lower L-shells than plasma sheet electrons [Foster, 1995]. Observational evidence for SAIDs includes satellite electric field measurements in the ionosphere [Smiddy et al., 1977; Maynard, 1978; Rich et al., 1980] and the magnetosphere [Maynard et al., 1980] as well as ion drift meter measurements in the ionosphere [Spiro et al., 1979].

[4] Recently, the large-scale observing capability of the Super Dual Auroral Radar Network (SuperDARN) [Greenwald et al., 1995; Chisham et al., 2007] has been utilized to study various characteristics of the subauroral electric fields [e.g., Makarevich and Dyson, 2007; Koustov et al., 2008; Kataoka et al., 2009; Makarevich et al., 2009]. A number of studies have focused on relatively high latitude observations, or intervals of only weakly enhanced ring current. Koustov et al. [2006], for example, reported King Salmon radar observations of $\sim 2 \text{ km s}^{-1}$ subauroral flows up to a few degrees of latitude wide in the pre-midnight sector. Their observations were made during relatively undisturbed conditions ($D_{\text{ST}} \sim -30 \text{ nT}$) at relatively high latitudes ($> 60^\circ$). In a number of their events the velocity maximum occurred during the recovery phase of a substom and coincided with the equatorward edge of the auroral oval. These flows tended to be embedded within the low-latitude portion of the dusk convection cell, but their data set did not extend to low enough latitudes to fully investigate their equatorward extent. Oksavik et al. [2006], on the other hand, presented observations of an extended interval of subauroral flows from the Wallops Island radar, located at a lower magnetic latitude than King Salmon. Their observations, spanning the midnight sector ionosphere, were from a quasi-steady interval of southward IMF and magnetospheric convection during which the storm-time index remained at modest values ($D_{\text{ST}} > -10 \text{ nT}$). Although they observed some variability in the velocity and latitudinal extent of the flows the only variation in the location of the flows was a gradual decrease in latitude with increasing local time. While this relatively ‘steady state’ event precluded any investigation of the effects of variable solar wind driving or impulsive

magnetotail activity it did suggest the existence of variability associated with processes internal to the magnetosphere-ionosphere system.

[5] In this paper we present an analysis of subauroral ionospheric electric field observations made during a geomagnetic storm that occurred in August 2010. We focus on data from the recently deployed Falkland Islands SuperDARN HF radar, which is the only southern hemisphere SuperDARN radar with a field-of-view covering the $50^\circ\text{--}60^\circ$ magnetic latitude range and thus capable of studying the subauroral region of the ionosphere even during expanded polar cap intervals such as geomagnetic storms. During the storm main phase the Sym-H index reached $\sim 80 \text{ nT}$ and the IMF was highly variable, resulting in an interval of dynamic magnetospheric activity including multiple substorms and auroral electrojet enhancements. We discuss the effects of the storm on the ionospheric conditions and describe a detailed study of a high velocity flow channel, which matches many of the characteristics of the SAID discussed above, and was observed almost continuously by the radar for over 6 hours as it traversed the pre-midnight sector. We also discuss coincident data from the low-altitude Defence Meteorological Satellite Programme (DMSP) satellites, and the magnetically near-conjugate northern hemisphere Blackstone SuperDARN radar. The Falkland Islands radar observations in particular are important for a number of reasons: (1) they consist of simultaneous, high-resolution measurements, spanning a range of magnetic local times at latitudes below $\sim 60^\circ$, (2) they were continuous for many hours despite occurring at the peak of storm activity and spanning a number of substom intensifications during which HF radars often observe limited scatter [Milan et al., 1999], (3) they were made concurrently with conjugate DMSP satellite and northern hemisphere HF radar observations allowing the broader characteristics of the subauroral flows to be inspected, and (4) they reveal a connection between the subauroral ionosphere and large-scale magnetospheric dynamics inferred from the evolution of the flows in concert with changes in the solar wind and magnetosphere. We find that variations in the latitude of the channel are related to changing conditions in the interplanetary magnetic field and auroral zones, while variations in its velocity were more closely related to ring current dynamics. These results suggest that the electrodynamics of the night-side subauroral region are driven both by processes occurring in the inner magnetosphere and the larger-scale effects of solar wind-magnetosphere coupling.

2. Instrumentation and Data Sets

2.1. SuperDARN

[6] The Super Dual Auroral Radar Network (SuperDARN) is an international array of HF coherent radars in the northern and southern hemispheres used in the study of various aspects of magnetospheric and ionospheric physics [Chisham et al., 2007]. In this study we utilize data from two of the radars, the primary focus being on data from the southern hemisphere Falkland Islands radar (FIR) with some supporting data provided by the northern hemisphere Blackstone radar (BKS). The FIR and BKS radars are located at geographic coordinates 51.8°S , 59.0°W and 37.1°N , 78.0°W , respectively. Both radars were operating in a stan-

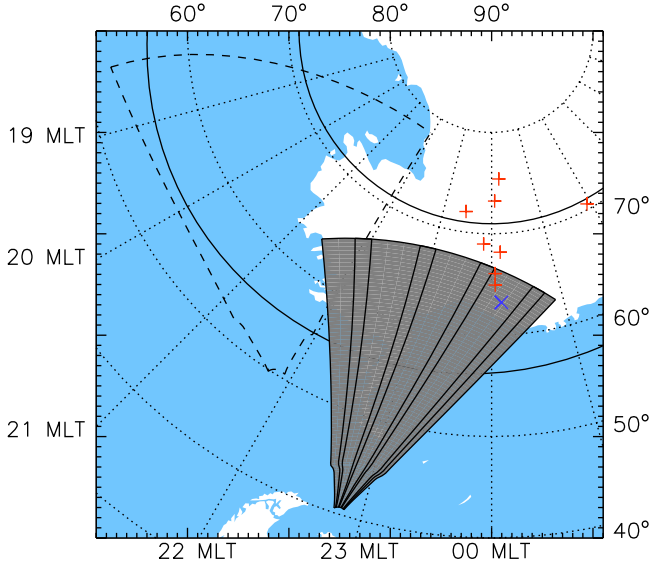


Figure 1. A map showing the field-of-view of FIR at 0300 UT on a magnetic latitude magnetic local time grid with dusk to the left and midnight to the bottom. Data from the four individual beams in the field-of-view (from left to right, beams 2, 6, 10 and 14) are discussed in the text. The mapped conjugate location of the northern hemisphere BKS radar field-of-view is indicated by the dashed line and a model auroral oval (for $K_p = 6$) [after Milan et al., 2010] is included for reference. The + and \times symbols indicate the locations of a chain of ground magnetometers.

dard mode during the study interval, in which they scan through 16 beams with a dwell time of 3 seconds on each, building up a full scan in ~ 1 minute. Each beam is divided into 75 range gates of length 45 km, and so in each 3 second sample the radars cover over 3000 km in range. The beam separation of FIR (BKS) is 3.24° (3.86°), giving a total viewing azimuth of $\sim 52^\circ$ ($\sim 62^\circ$) in each full scan. Taking into account their different locations and pointing directions this results in the fields-of-view of both radars spanning ~ 3 h of magnetic local time at a latitude of $\sim 55^\circ$, where the primary observations in this study are made.

[7] A map showing the field-of-view of FIR at 0300 UT (the central time of a key interval discussed below) is shown in Figure 1, on a magnetic latitude – magnetic local time grid with dusk to the left and midnight to the bottom. The coordinates used are Altitude Adjusted Corrected Geomagnetic (AACGM) coordinates, a development of the PACE system discussed by Baker and Wing [1989]. Data from the four individual beams shown on the field-of-view (from left to right, beams 2, 6, 10 and 14) are discussed below. Use of the AACGM coordinate system enables the magnetically near-conjugate northern hemisphere BKS radar field-of-view to be directly compared on the same map and this is indicated by the dashed outline. A model auroral oval (for $K_p = 6$) [after Milan et al., 2010] is included for reference. The + and \times symbols correspond to the locations of a chain of ground magnetometers and are discussed below.

2.2. ACE Spacecraft

[8] Solar wind data at 64 s resolution and interplanetary magnetic field data at 16 s resolution have been provided by

the Solar Wind Electron Proton Alpha Monitor [McComas et al., 1998] and Magnetic Field Experiment [Smith et al., 1998], respectively, on-board the Advanced Composition Explorer (ACE) spacecraft [Stone et al., 1998]. Throughout this paper the IMF data are presented and discussed in terms of their geocentric solar magnetospheric (GSM) coordinates. Data from both instruments have been used to estimate the travel time between features being observed by the ACE spacecraft and them arriving at Earth, according to the method of Khan and Cowley [1999]. This time delay has then been added to the time series of data presented in the subsequent sections to enable direct comparison with ground-based data. The ACE data have also been used to estimate the dayside reconnection rate, V_D , according to Milan et al. [2007] using the equation:

$$V_D = v_{SW} B_\perp L \sin^4(\theta/2), \quad (1)$$

where v_{SW} is the solar wind speed, B_\perp is the component of the magnetic field perpendicular to the Earth-sun line, θ is the IMF clock angle (measured clockwise from north), and L is the width of the dayside reconnection line, taken to be $5 R_E$. This value is consistent with the range suggested by Milan et al. [2007] but, as will be discussed in section 4.1, the choice of L does not critically affect our predominantly qualitative interpretation.

2.3. Geomagnetic Data

[9] Two sets of geomagnetic indices have been utilized in this study to monitor the global level of geomagnetic activity. The Dynamic Storm Time (D_{ST}) index [Sugiura, 1964] is obtained from magnetometer stations near the equator where the northward disturbance field is dominated by the intensity of the ring current. We use a high time-resolution version of this index, Sym-H [Iyemori and Rao, 1996], as recommended by Wanliss and Showalter [2006], which is the average at all local times of the deviation of the H -component from a quiet day. We also consider the Asym-H index, which is the difference between the largest and smallest values of the different local time measurements used in the calculation of Sym-H and therefore gives a measure of ring current asymmetry. An asymmetric, or partial ring current arises following injections of hot ions from the tail, which drift into the evening and afternoon sectors [Weygand and McPherron, 2006], and closes in the ionosphere via field-aligned-currents at dusk and dawn [Cowley, 2000]. Enhancements in Asym-H therefore provide an indication of substorm injections and field-aligned-current systems.

[10] To provide an overview of concurrent auroral activity we use the auroral electrojet indices [Davis and Sugiura, 1966], derived from a chain of ground magnetometers distributed in local time at typical auroral latitudes. AU represents the envelope of maximum northward disturbance measured at all stations (indicative of the eastward electrojet) and AL represents the envelope of minimum (maximum negative) disturbance (usually indicative of the westward electrojet). The latter is also influenced by the substorm current wedge, which further enhances the westward electrojet in the midnight sector. To help distinguish the substorm electrojet component of AL from the convection electrojet we also show H-component magnetic field data

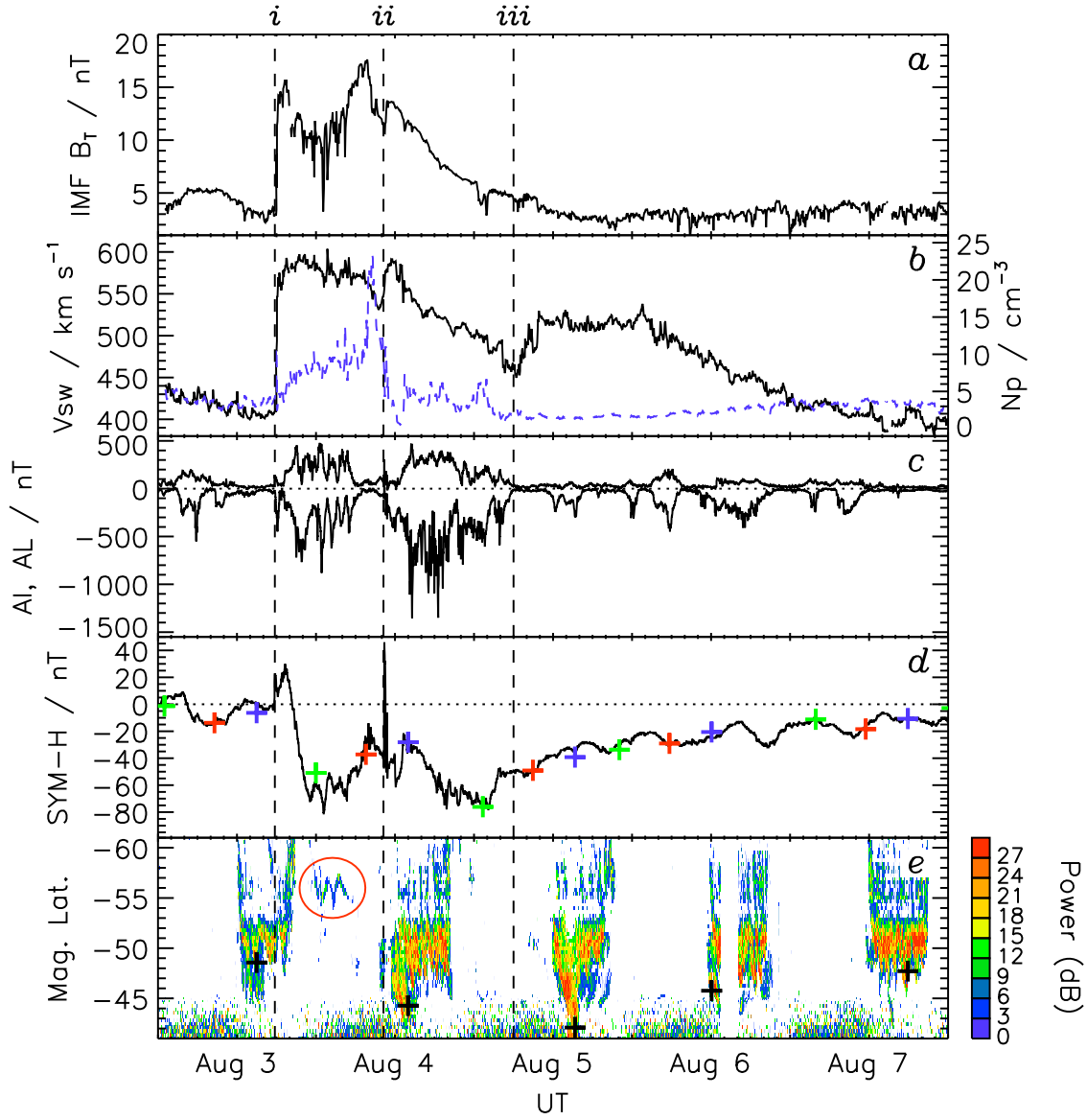


Figure 2. Time series of data from 0000 UT on 3 August to 0000 UT on 8 August 2010 for (a) IMF magnitude, (b) solar wind velocity (black/solid) and number density (blue/dashed), (c) auroral electrojet indices (AU and AL), (d) Sym-H index, and (e) backscattered power from beam 6 of FIR, plotted versus magnetic latitude. The backscattered power is scaled according to the color bar on the right. The crosses shown in Figures 2d and 2e, and the circled patch of scatter in Figure 2e, are discussed in the text. The vertical dashed lines indicate times of interest discussed in the text.

from a set of magnetometers close to the FIR field-of-view. Filtered (20–200 s) data, providing evidence of impulsive Pi2 band wave activity typically associated with substorm onsets, are also presented. The locations of these magnetometers are indicated by the + and \times symbols on Figure 1.

2.4. DMSP Spacecraft

[11] Measurements of ion and electron fluxes by the SSJ/4 instrument on board the Defence Meteorological Satellite Programme (DMSP) F16, F17, and F18 spacecraft [Hardy *et al.*, 1994] have been employed to examine the patterns of auroral particle precipitation and their relationship to the plasma flow. The instrument points toward zenith at all times, and provides 1 s resolution spectra of ion and electron

fluxes between 30 eV and 30 keV. Measurements of plasma bulk velocity provided by the DMSP Thermal Plasma Experiment Driftmeter instrument have also been employed to augment the radar observations. This instrument measures the two components of the plasma drift velocity along two axes perpendicular to the spacecraft's velocity vector.

3. Observations

3.1. Storm Overview

[12] Figure 2 presents an overview of the geomagnetic storm that occurred during 3–8 August 2010. Figure 2a shows the IMF magnitude and Figure 2b the solar wind velocity (black/solid) and number density (blue/dashed).

These data are plotted with the time delay described in section 2.2 applied. Figures 2c and 2d show the auroral electrojet indices (AU and AL), and the Sym-H index, respectively. Figure 2e shows backscattered power from beam 6 of FIR, plotted versus magnetic latitude, scaled according the color bar on the right.

[13] The solar wind data indicate the arrival of a fast solar wind front at the Earth at \sim 1840 UT on 3 August (*i*), across which its speed increased from \sim 400 km s $^{-1}$ to almost 600 km s $^{-1}$ and the IMF strength increased by more than 10 nT. This appears to have triggered a geomagnetic storm, evidenced by a subsequent \sim 100 nT decrease in Sym-H, and a series of enhancements in auroral activity seen in the AU and AL indices. A second enhancement in the solar wind and IMF strength \sim 16 h later (*ii*) was associated with a subsequent interval of enhanced auroral activity and an intensification in the Sym-H storm main phase. A third increase in solar wind speed occurred \sim 20 h later (*iii*) that was not, however, accompanied by a significant IMF magnitude enhancement and was followed by much weaker auroral activity. After this time the storm recovery phase began and over the course of the next \sim 2 days the solar wind speed and Sym-H index returned to prior conditions.

[14] The radar data shown in Figure 2e reveal 5 latitudinally broad intervals of scatter from between \sim 1200 UT and \sim 2000 UT on each day. Analysis of the velocities and spectral widths revealed by these data indicate that they represent scatter not from the ionosphere but from the ground. These data, and the crosses superposed on them and on the Sym-H data, are discussed further in section 4.2. The latitudinally narrow region of radar backscatter observed at \sim 55°S between midnight and 0600 UT on 4 August (circled in red), on the other hand, is ionospheric scatter of considerable velocity and this is considered in more detail in the next section.

3.2. Storm Main Phase

[15] Figure 3 presents a restricted time series of data from the storm sudden commencement and main phase, from 1600 UT on 3 August to 0900 UT on 4 August 2010. Figure 3a shows the three GSM components of the IMF (B_X in blue, B_Y in green, and B_Z in red) and Figure 3b the solar wind velocity (black/solid) and number density (blue/dashed). In this case, the time shift applied to the data discussed in section 2.2 has been adjusted by 6 minutes such that the solar wind velocity enhancement is coincident with a storm sudden commencement signature discussed below. Figure 3c shows the auroral indices in the same format as in Figure 2, and Figure 3d shows unfiltered (back/solid) and filtered (20–200 s) (blue/dashed) H-component data from the magnetometer shown in Figure 1 by the blue \times symbol. Figure 3e shows the Sym-H (black/solid) and Asym-H (blue/dashed) indices, scaled according to the left and right hand side axes, respectively. Note that although these two axes differ in range they do correspond to the same scale. Figure 3f shows the line-of-sight Doppler velocity of ionospheric backscatter targets from beam 6 of FIR, plotted on a reduced magnetic latitude scale compared to Figure 2e, to highlight the latitude variation of the flows. The velocity scale, represented by the color bar on the right, shows only negative velocities indicative of the predominance of flows directed away from the radar (poleward) on this beam.

[16] These data clearly reveal that the storm main phase was initiated with a sharp 20 nT increase in Sym-H (*i*) (the so-called storm sudden commencement, or SSC). The ACE data show that during the \sim 3 h following this the IMF strengthened and underwent considerable reorientation before settling in a predominantly southward direction ($B_Z \sim -10$ nT) at \sim 2030 UT (*ii*). It remained in this orientation for \sim 3 h, during which time the Sym-H magnitude increased steadily, Sym-H reaching \sim 70 nT by the time of a brief northward excursion of the IMF at \sim 2330 UT (*iv*). Over the early part of this interval (*ii–iii*), during which a substorm onset was observed in the ground magnetometer data (evidenced by the large amplitude (\sim 150 nT) Pi2 signature and magnetic bay), Asym-H increased rapidly from \sim 40–120 nT.

[17] During the latter part of the interval (*iv–v*) the main phase of the storm progresses with little variation in Sym-H. The auroral and Asym-H indices, however, as well as filtered and unfiltered magnetometer data, indicate the occurrence of a subsequent series of substorms and auroral intensifications. These intensifications coincided with a series of north-south rotations of the IMF and slight decreases (10–20 nT) in the Sym-H index and their significance is discussed further in section 4. The narrow channel of ionospheric scatter observed by FIR was also coincident with this interval and exhibited high line-of-sight velocity magnitudes (\sim 100–1000 m s $^{-1}$) and an oscillatory motion in the magnetic latitude of its location of 2°–3°. After (*v*) the IMF orientation changed again, becoming strongly northward, auroral electrojet activity declined and the storm began to recover. The next section focusses on the radar data in the interval between (*iv*) and (*v*).

3.3. Location of the Flow Channel

[18] Before looking in detail at the flows within the channel it is important to understand its geometry and geophysical location. Figure 4 therefore presents two snapshots of the FIR line-of-sight velocity data (Figure 4a), plotted in magnetic latitude – magnetic local time coordinates, from 0119 UT and 0301 UT on 4 August 2010 and scaled according to the color bar on the right. The concentric dotted circles on each plot correspond to 10° intervals of magnetic latitude (starting from 40°S) and the radial dotted lines represent 1 h intervals of magnetic local time. These data give an impression of the magnetic local time extent of the channel, as well as how the magnitude and direction of the line-of-sight velocities vary across the radar field-of-view. In general, red colored scatter (corresponding to strongly negative Doppler velocities, away from the radar) is observed in the westward pointing beams and blue colored scatter (corresponding to strongly positive Doppler velocities, toward the radar) in the eastward pointing beams. This is consistent with an overall westward and slightly poleward sense to the flows as will be discussed in the next section.

[19] Superposed on the radar data are plotted overpasses of the DMSP F18 satellite, colored with electron spectrogram data also shown in Figure 4b below, with Figure 4c showing the corresponding ion energy spectrograms. The white curves also superimposed on Figure 4b represent cross-track velocity data from the driftmeter instrument, the scale of which, in m s $^{-1}$, is identical to the scale of the electron energy axis. These data are discussed further below.

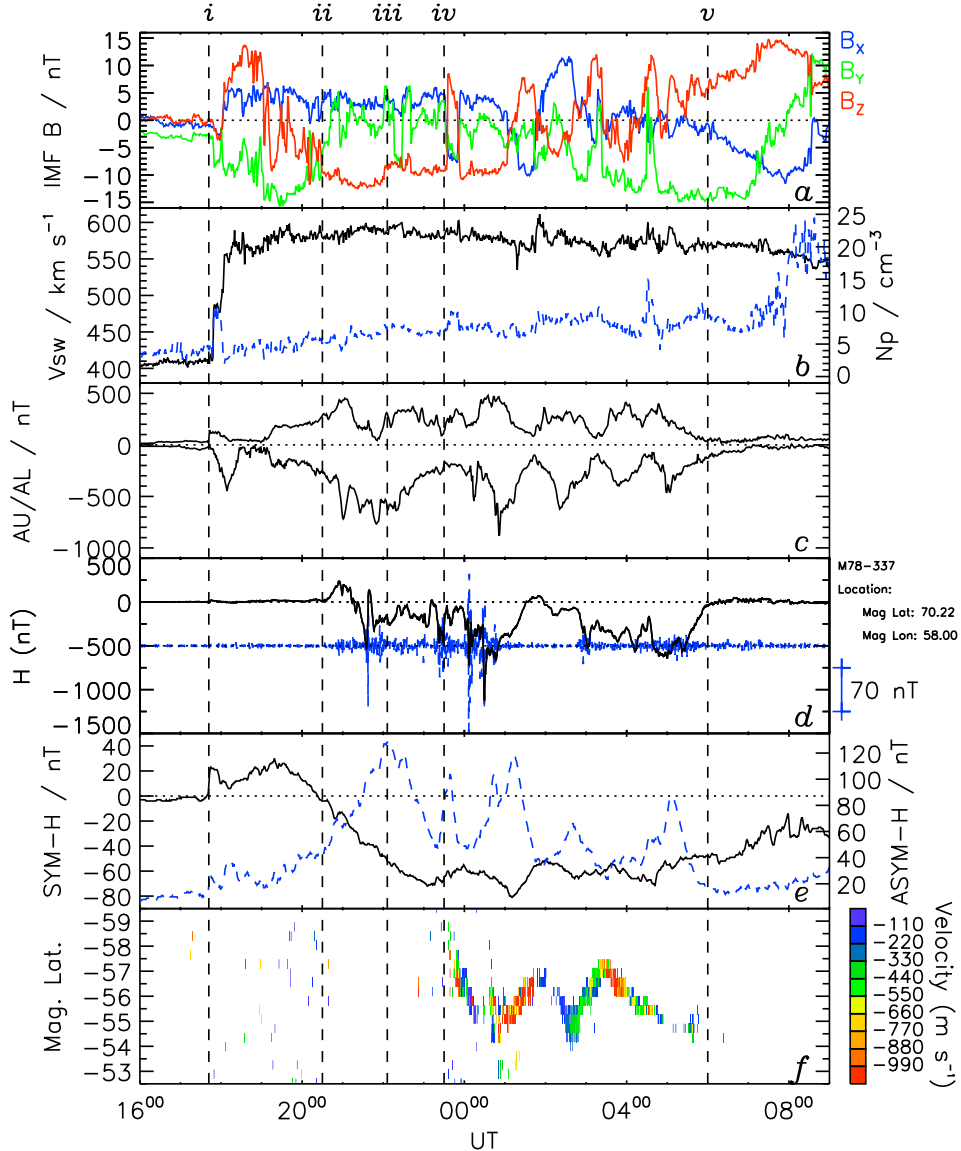


Figure 3. Time series of data from 1600 UT on 3 August to 0900 UT on 4 August 2010 for (a) the three GSM components of the IMF (B_X in blue, B_Y in green, and B_Z in red), (b) solar wind velocity (black/solid) and number density(blue/dashed), (c) the auroral electrojet indices (AU and AL), (d) unfiltered (black/solid) and filtered (20–200 s) (blue/dashed) magnetometer data from the station marked with the blue \times in Figure 1, (e) the Sym-H (black/solid) and Asym-H (blue/dashed) indices, and (f) line-of-sight Doppler velocity measurements from beam 6 of FIR, plotted versus magnetic latitude. The velocity of the flows is scaled according to the color bar on the right. The vertical dashed lines indicate times of interest discussed in the text.

The vertical dashed lines on the spectrograms in Figures 4b and 4c indicate the cut-off time of the precipitation in each case; as can be seen, for the second interval there is an offset between the two (discussed further below). The corresponding latitudes of the DMSP spacecraft at these cut-off times have been used to derive the boundaries (illustrated for the electrons (ions) by the thick black (grey) curves) in Figure 4a, by fitting to a circle offset from the pole by 4° toward midnight. This offset is based on a number of studies of auroral configuration [e.g., *Milan et al.*, 2010], which show the average auroral location to be shifted in this way, and also proves to be consistent with subsequent analyses

discussed later in this paper. The boundaries have been identified as corresponding to the maximum rate of change in the mean energy flux, within the latitude range 50° to 60° . For the ions the whole energy range was used to determine the mean but for the electrons, which appear to be energy dispersed, we have used only the lower end of the energy range. In fact, the lowest two energy bands appeared to be contaminated during a number of passes, indicating high fluxes along much of the spacecraft trajectory, so we have therefore used the mean of the 3rd and 4th energy bands, equivalent to the energy range 40 to 80 eV. Although this choice is somewhat arbitrary, the difference in latitude that

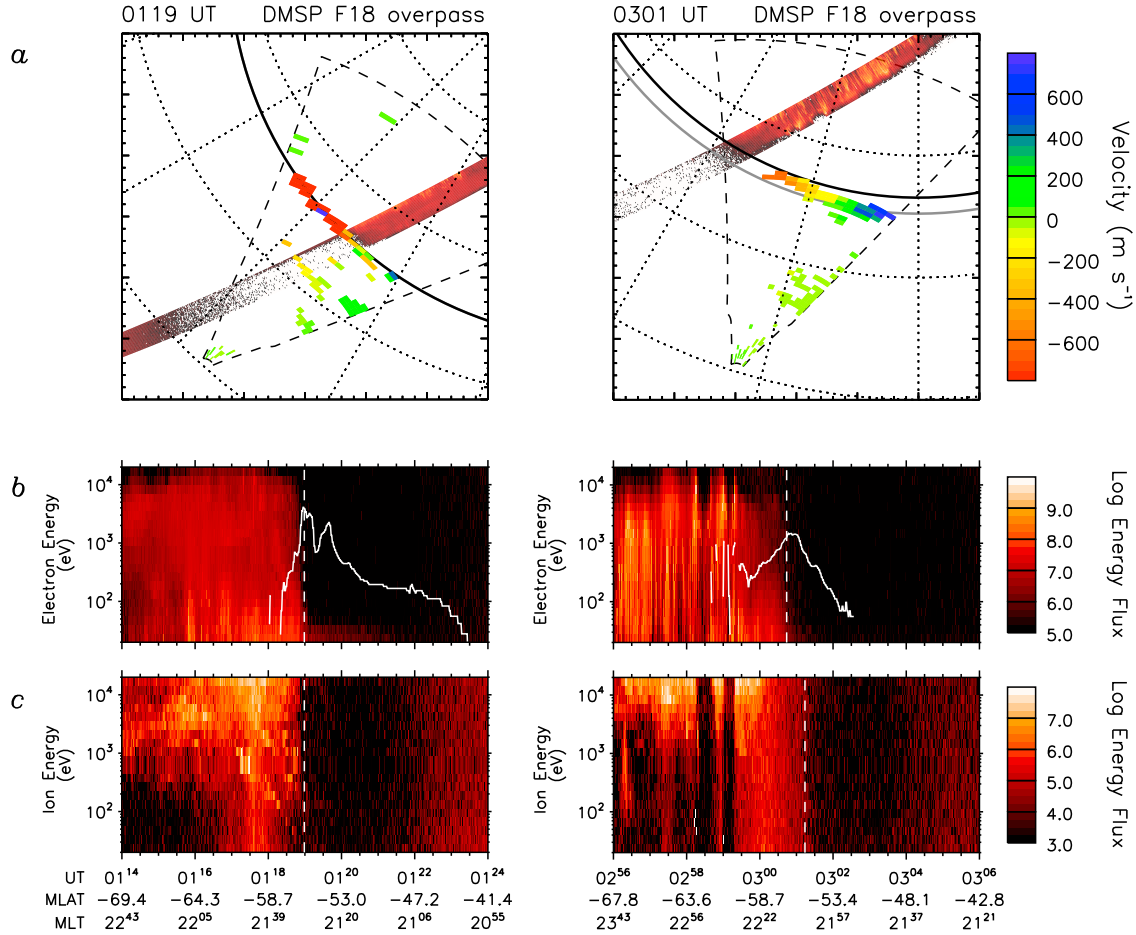


Figure 4. (a) Polar plots of FIR line-of-sight Doppler velocity measurements overlaid with electron energy spectra from the DMSP F18 satellite. The velocity of the flows is scaled according to the color bar on the right, and the electron energy spectra according to the bar on the right of Figure 4b. The thick curves represent the electron (black) and ion (grey) precipitation boundaries and their derivation is discussed in the text. (b) Electron and (c) ion energy spectrograms from the DMSP F18 satellite, with the location of the precipitation boundaries marked by the black and white dashed lines. The energy flux in each case is scaled according to the color bar on the right of each panel. The white curves on Figure 4b represent velocity data from the driftmeter instrument to the same scale, in m s⁻¹, as the electron energy axis.

would be derived using adjacent energy bands is only of the order of a fraction of 1° and therefore not considered significant in our subsequent interpretation.

[20] A number of additional overpasses by this and two other DMSP spacecraft occurred during the interval of study, and a similar analysis to that described above in reference to Figure 4 has been conducted for those also. The results of these analyses are shown in Figure 5, which presents the backscatter latitude from FIR beam 6 from 2330 UT on 3 August to 0600 UT on 4 August 2010. Superposed are crossings by the 3 DMSP satellites, where the center of each bar corresponds to the universal time-magnetic latitude position of the spacecraft. The latitudes of these crossings have been adjusted according to the modeled boundary circle described above, to account for the offset between the magnetic local time of the radar backscatter and the spacecraft. In Figure 5 (top) the full range of the electron energy spectra are shown (as in Figure 4), with the corresponding ion energy spectra shown in the second panel.

Both are scaled according to their respective color bars on the right. In the third panel the mean ion and electron energy fluxes from the energy bands discussed above are shown; for each pass the electron data are on the left and the ion data on the right. Superposed on these passes are the cut-off boundaries as described above; the electron boundaries are shown by the + symbols and the ion boundaries by the × symbols. These data show that the location of the flow channel is either close to, or just equatorward of, the electron precipitation boundary and almost always poleward of the ion precipitation boundary. This is discussed further in section 4, below.

[21] In Figure 5 (bottom) the DMSP F16 and F18 crossings are colored according to the driftmeter velocity measurements mentioned above, scaled according to the color bar on the right (no suitable data exist from the F17 satellite). Subsequent analysis (discussed in section 3.4) shows that the DMSP instrument was closely aligned with the direction of the flows within the channel and therefore provides a

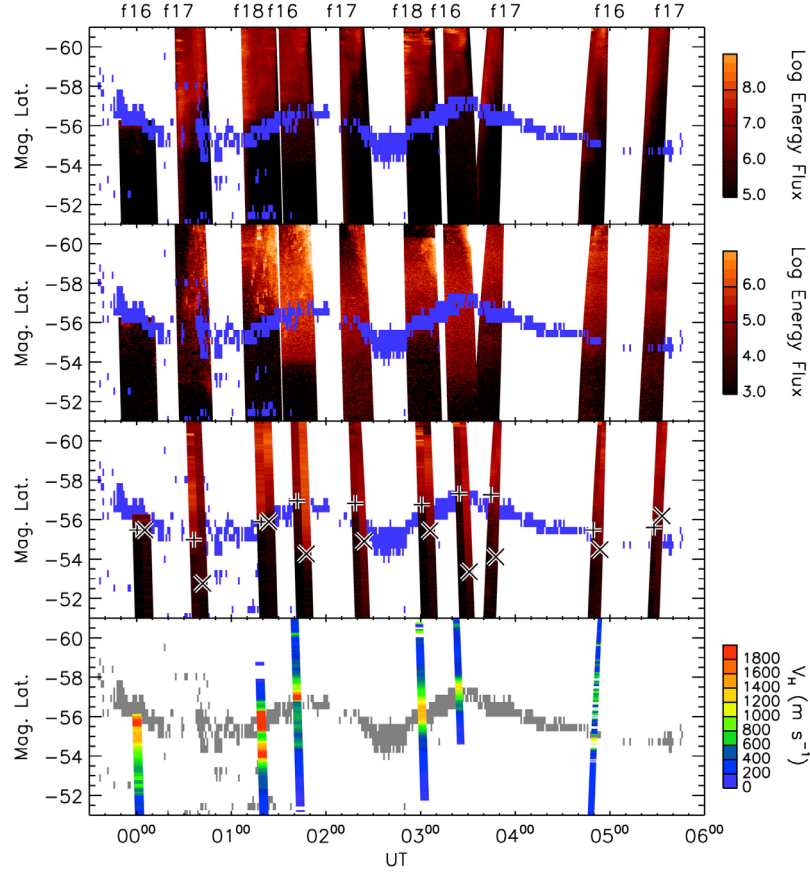


Figure 5. Time series of the FIR ionospheric backscatter data versus magnetic latitude from 2330 UT on 3 August to 0600 UT on 4 August 2010. Superposed are crossings by the DMSP satellites, where the center of each bar corresponds to the time-latitude position of the spacecraft. (top) The full range of the energy spectra is shown, with the corresponding ion spectra shown in the second panel, both scaled according to their respective color bars on the right. In the third panel mean values from selected energy bands are shown (as discussed in the text) with electron boundaries identified by the + symbols and ion boundaries by the \times symbols. (bottom) The bars are color coded to velocity measured by the driftmeter instrument, scaled to the color bar on the right.

good indication of the magnitude of the flows. These data also corroborate the location of the channel as identified by the radar but reveal that at times the channel sat in a broader, lower velocity, region of enhanced flow. This is also evident in, for example, Figure 4 (left). The data superposed in white on the electron spectrogram show the velocity to have been in excess of 1000 m s^{-1} over a few degrees of latitude close to the precipitation boundary, and then to have remained elevated at over 100 m s^{-1} as the spacecraft traversed another $\sim 10^\circ$. These observations are consistent with the idea that the narrow, high speed flow channel observed by FIR is a SAID, embedded within the broader, slower, flows of the SAPS [e.g., *Foster and Burke*, 2002].

[22] Last in respect to the flow channel location, we investigated the interhemispheric location of the flow channel by inspecting data from SuperDARN radars in the northern hemisphere. The Blackstone SuperDARN radar (BKS), located close to the geomagnetic conjugate point of FIR, observed limited backscatter during the interval, but did capture the flow channel in the early part. Two examples of simultaneous observations are presented in Figure 6, which shows polar plots, similar to those in the upper panels

of Figure 4, from 0045 UT and 0300 UT on 4 August 2010. Line-of-sight velocity data from both radars are shown together (according to the mapping discussed in section 2.1) and illustrate that fast flows occurred simultaneously and at similar latitudes in both hemispheres. The main difference between the BKS observations and those made by the FIR is that the region of ionospheric backscatter is wider, most noticeably in the 0300 UT map. The high-speed element of the channel is a similar width, but lower velocity backscatter is also observed equatorward of this. This is consistent with the DMSP driftmeter observations, discussed above, regarding the SAID-SAPS relationship.

3.4. Velocity in the Flow Channel

[23] Having established the geometry and location of the flow channel, we now turn to investigate the time-variability of the observations in more detail. Figure 7 presents FIR line-of-sight velocity data from the interval 2330 UT on 3 August to 0600 UT on 4 August 2010. A magnetic latitude-time-velocity plot is shown in Figure 7a for each of the four beams indicated in Figure 1, color-coded according to the bar on the right. The near-vertical dashed line on each plot

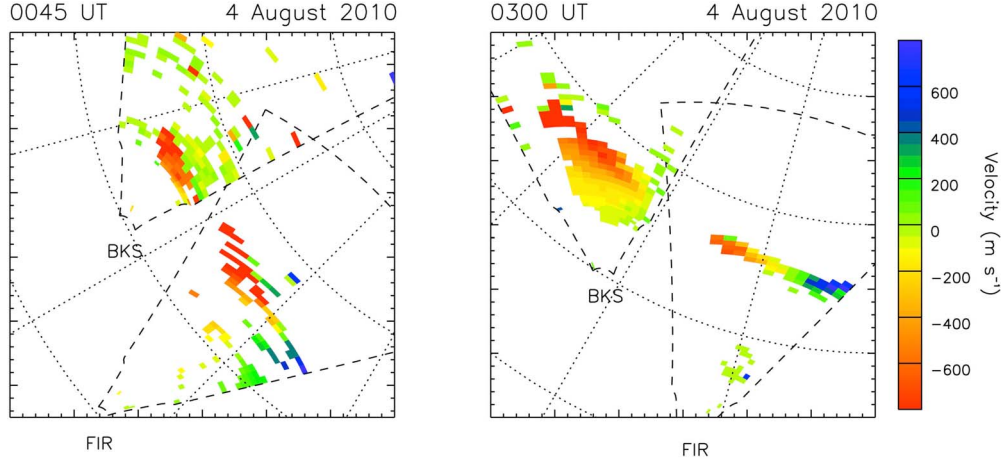


Figure 6. Polar plots of line-of-sight Doppler velocity measurements from FIR and BKS from (left) 0045 UT and (right) 0300 UT on 4 August 2010. The velocity of the flows is scaled according to the color bar on the right.

indicates the UT of midnight magnetic local time. Over the course of the interval there is considerable variability, in both the latitude and velocity of the flows, evident in the data from all four beams; this is discussed in detail in section 4. There is also evidence of variability across the radar field-of-view such that, with increasing beam number

(and therefore increasing magnetic local time), the velocities evolve from strongly negative to positive and the latitude of the flow channel as a whole moves equatorward. This latitude variation is in agreement with previous observations of SAID discussed in section 1 and with our observations shown in section 3.3. The velocity variation is due to the

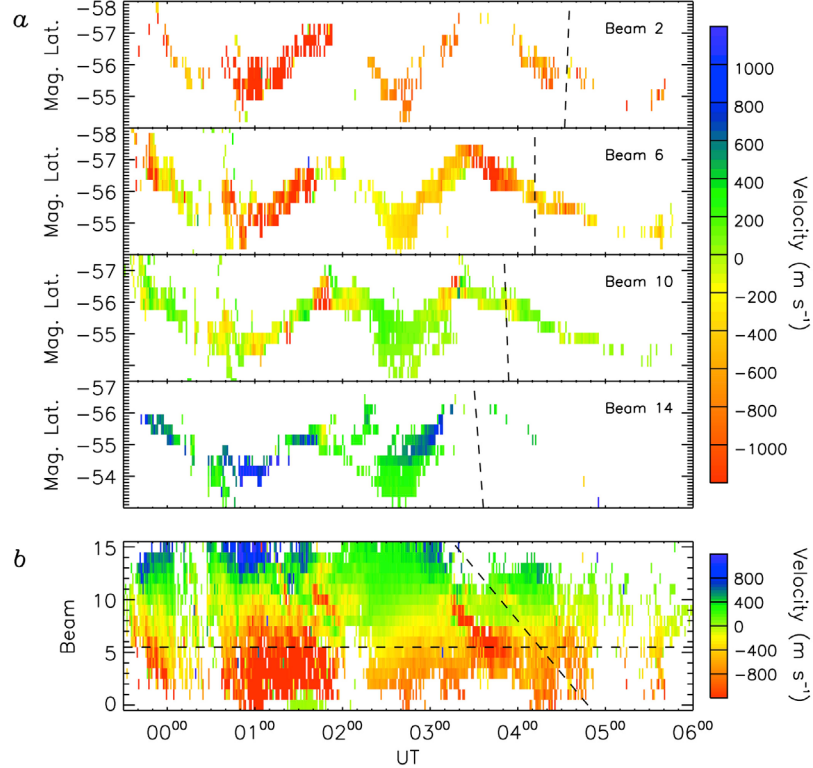


Figure 7. (a) Four single-beam magnetic latitude-time-velocity plots from beams 2, 6, 10, 14 (top 4 panels) and (b) a beam-time-velocity plot of FIR line-of-sight velocity data from the interval 2330 UT on 3 August to 0600 UT on 4 August 2010. The near-vertical dashed line on each panel in Figure 7a indicates the approximate UT of midnight magnetic local time. In Figure 7b the meridional direction is indicated by the horizontal dashed line and midnight magnetic local time approximated by the diagonal dashed line.

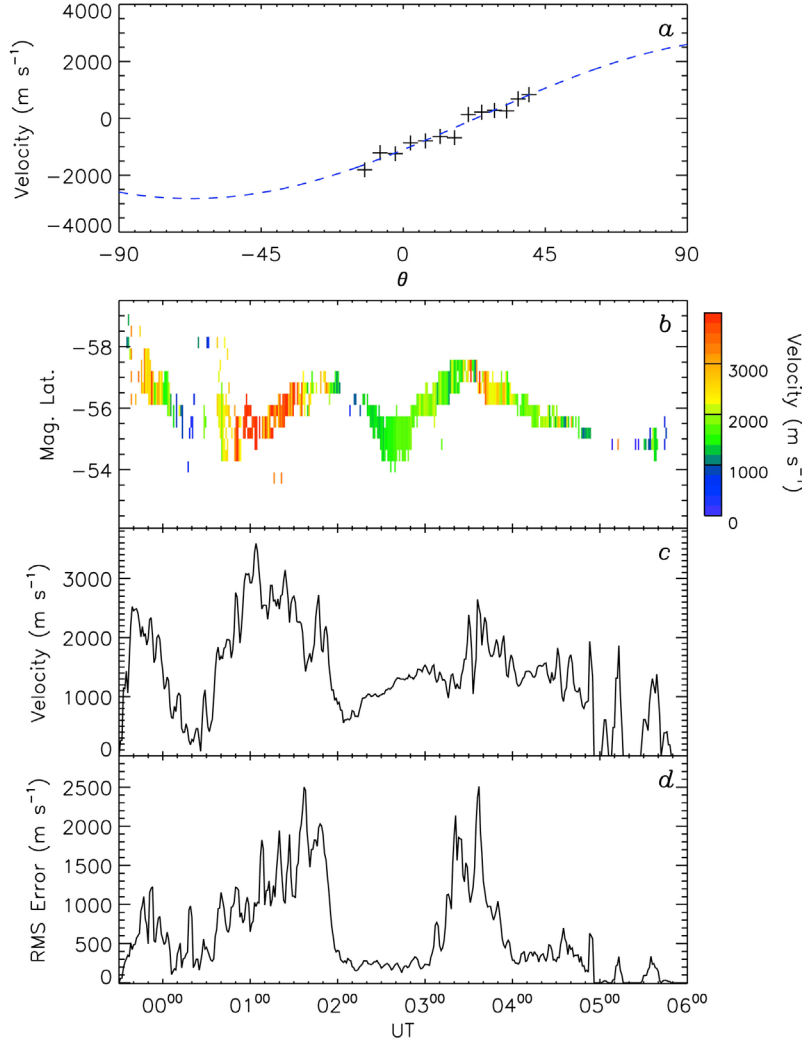


Figure 8. (a) FIR line-of-sight velocity data, from 0130 UT on 4 August 2010, plotted versus beam azimuth, θ , (+ symbols) and corresponding best fit (blue/dashed curve). (b, c) Time series velocity data from FIR from the interval 2330 UT on 3 August to 0600 UT on 4 August 2010, derived using the fitting technique illustrated in Figure 8a. (d) The RMS error of Figures 8b and 8c.

geometry of the radar beams, also discussed in section 3.3, and is considered further below.

[24] Figure 7b presents a beam-time-velocity plot in which the mean velocity across the latitudinal width of the flow channel is plotted at each time step for each beam. In this panel the meridional direction is shown by the horizontal dashed line and the approximate universal time at which each beam intersects midnight magnetic local time is indicated by the diagonal dashed line. As illustrated in Figure 1 beams at earlier MLTs are directed slightly westward and beams at later MLTs are directed slightly eastward. These data highlight the fact that, in general, the westward directed beams measure negative velocities, while the eastward directed beams measure weaker negative, or positive, velocities. This implies that the flows were predominantly westward directed across the entire radar field-of-view. The lowest velocities were seen, on average, in beam 10 of the radar, the pointing direction of which has an azimuth of $\sim 20^\circ$. Assuming that this beam was therefore closest to the direction perpendicular to the direction of

flow, this implies an azimuth of the average flow vector of $\sim 70^\circ$. This is consistent with the average flow vector being close to the direction parallel to the flow channel itself, which was also oriented in a slightly poleward (south) of west direction as illustrated in Figure 4.

[25] If we assume that the velocity of the channel is constant along its length, which seems at least on average to be true, it is possible to use the measurements from different beams to estimate the true velocity vector. This is illustrated in Figure 8a, which shows FIR line-of-sight velocity measurements from 0130 UT plotted versus θ , where θ is the corresponding azimuthal angle of each beam with respect to geomagnetic north. By fitting to the expected sinusoidal variation of velocity with beam azimuth the magnitude of the velocity vector can be inferred from the amplitude of the fit. This has been applied at each time step and the results are presented in Figures 8b and 8c. Figure 8b presents this velocity plotted according to the magnetic latitude of the beam 6 backscatter location in a similar format to Figure 3f, and Figure 8c shows it plotted as a simple line plot. The data

in Figure 8b reflect the general trend of how the velocity changes with the associated latitude variation of the channel. These data, and those in Figure 8c, suggest that while the velocity exhibits variability over the interval on similar timescales to the latitude variations, there is no one-to-one relationship between the two. This implies that the physical process responsible for driving the electric fields within the channel might be different to the process causing the latitude variations.

[26] Our assumption of constant velocity along the flow channel's length is of course not strictly true, and the existence of variability implies structure which may be physically significant. The data presented in Figure 8d provide a measure of this variability in the form of the RMS error of the fits illustrated in Figure 8a. The implications of these data become evident if we compare them to the data in Figure 7b. Consider, for example, 0240 UT where the velocity measured by the radar varied smoothly across all beams. This time corresponds to a low value of RSM error. At 0330 UT on the other hand, where a small-scale perturbation is evident across the beams in Figure 7b, the RMS error in the fit is significantly higher. Interestingly, the peaks in RMS error appear to coincide with the peaks in the latitude of the channel, suggesting that there is more structure in the flow channel at higher latitudes than at low latitudes. This idea is revisited in section 4.

4. Discussion

4.1. Ionospheric Electrodynamics

[27] In section 3 we have reported on observations of a fast flow channel observed by the Falkland Islands SuperDARN radar on 3–4 August 2010. This feature resembles prior observations of subauroral electric fields, in particular of subauroral ion drifts, or SAID. Anderson *et al.* [1993] suggested a mechanism for the formation of SAID which we summarize here. Following substorm onset the equatorward boundaries of the ion and electron precipitation separate, with the ions moving well equatorward of the electrons in the pre-midnight sector. The equatorward extent of the ion precipitation is coincident with the equatorward extent of the downward directed, region 2 field-aligned currents which close via Pedersen currents with the outward flowing region 1 currents at higher latitudes. Therefore the Pedersen currents flow in the region of low conductivity equatorward of the electron precipitation, and a broad region of relatively large, poleward-directed electric fields is produced. These electric fields in turn produce relatively large westward ion drifts observed in the form of the SAID.

[28] The ground magnetometer data presented in Figure 3 support the idea that the SAID observed during our interval was initiated following an interval of substorm activity, and that its persistence over many hours could be due to subsequent activations in the tail. The DMSP data are also consistent with this mechanism in showing that the SAID was generally located between the ion and electron precipitation equatorward boundaries. Anderson *et al.* [1991] reported a number of fundamental properties of SAID structures in the ionosphere derived from satellite data and concluded that an individual SAID event lasts between 30 min and 3 hours and that their latitudinal extent becomes narrower as the event progresses. They also found that the

plasma flow associated with the SAID events is almost always westward in the pre-midnight sector. These findings are consistent with our results, and could explain the separated intervals of enhanced flows evident in Figures 8b and 8c. If an individual SAID event lasts only of the order 3 h then our interval could consist of a number of SAID events, possibly related to individual substorm intensifications. They might also explain the thinning of the flow channel to the point of it briefly disappearing from the radar data altogether, as is apparent in Figure 8b at ~0030 UT, ~0200 UT, and ~0500 UT, if this corresponded to the transition between one SAID and another.

[29] To facilitate an analysis of the time variability observed in our data we reproduce a subset of the observations from section 3 in Figure 9, which presents time series data from 2330 UT on 3 August to 0600 UT on 4 August 2010. The FIR beam 6 backscatter is reproduced in Figure 9a along with the + and × symbols representing the DMSP boundary locations from Figure 5. To provide a simple measure of the latitude of the SAID, Λ_S , we have determined the median location of the FIR backscatter in the range 52°–60°S and this is shown by the black line in Figure 9a. This estimate of Λ_S (or 90° – Λ_S where a comparison with SAID co-latitude is more appropriate) is also superimposed in red on subsequent panels. In Figure 9b we reproduce the estimated velocity magnitude, vel_S (black/solid curve) and variability, var_S (blue/dashed curve) from Figures 8c and 8d. Ground magnetometer data is presented in Figure 9c, in this case from all of the magnetometers indicated in Figure 1, plotted versus the approximate magnetic latitude of the station, and color coded according to the scale on the right. From Figure 3 we reproduce the auroral indices (black curves) in Figure 9d and the Sym-H index (black/solid curve) and Asym-H index (blue/dashed curve) in Figure 9e. Note that the y-axis for Sym-H in this case has been reversed, such that we can easily compare Sym-H and Asym-H magnitude. Last, in Figure 9f, are estimates of the dayside reconnection rate, V_D (black/solid curve), and integrated flux (blue/dashed curve); these are discussed in more detail below. All of these data (with the exception of that from the DMSP overpasses) have been resampled to the time-resolution of the solar wind data (64 s), the lowest resolution time series, to facilitate subsequent analyses, discussed below.

[30] The most striking feature of the data sets presented in Figure 9 is the variability that they exhibit over relatively short timescales and the similarity between the variations in each case. To investigate this similarity quantitatively we have performed a series of linear Pearson correlation analyses of both Λ_S and vel_S with a number of the other data sets presented in Figure 9. The $|H|$ parameter corresponds to the magnitude of the H-component disturbance measured by the magnetometer shown in Figure 1 by the blue × symbol. We also include a V_D^* parameter, corresponding to V_D with a 20 min time-lag imposed, which we discuss later. The results of these analyses are given in Table 1 with the correlation coefficient, r , and corresponding uncorrelated probability, p , being quoted in each case. A positive value of r indicates correlation with SAID latitude and a negative value implies a correlation with SAID co-latitude. The uncorrelated probability, that is, the probability that two uncorrelated variables would yield a given value of $|r|$, is

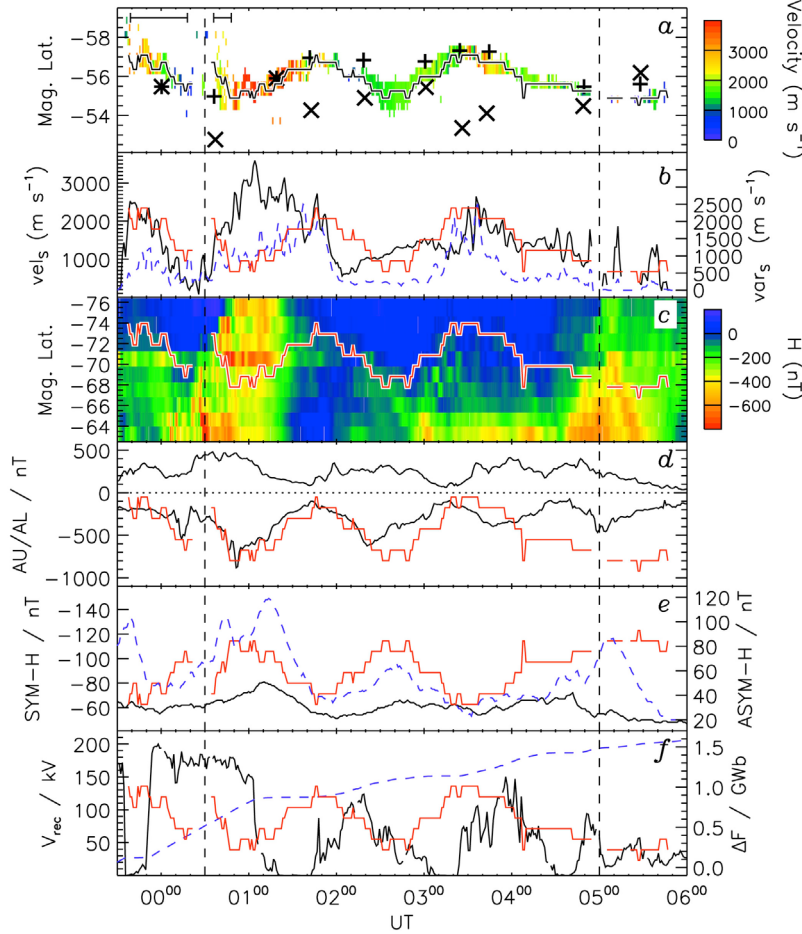


Figure 9. Time series of data from 2330 UT on 3 August to 0600 UT on 4 August 2010 showing (a) backscatter from beam 6 of FIR, plotted versus magnetic latitude. The + and × symbols representing DMSP boundary locations from Figure 5 are reproduced here and the black line is the median location of the FIR backscatter in the range 52° – 60° S. The two horizontal bars mark regions of backscatter discussed in the text. (b) Estimated total velocity, vel_s (black/solid) and variability var_s values (blue/dashed) from Figure 8. (c) The latitude-time distribution of H-component data from the chain of magnetometers shown in Figure 1. (d) Auroral electrojet indices (AU and AL) (black/solid). (e) The Sym-H (black/solid) and Asym-H (blue/dashed) indices. (f) The inferred dayside reconnection voltage (black/solid) and integrated flux (blue/dashed) as described in the text. The red curves on Figures 9b–9d and 9f correspond to the backscatter latitude from Figure 9a, shown on an arbitrary y-axis. The red curve on Figure 9e corresponds to the backscatter colatitude. The vertical dashed lines delimit a subinterval of interest discussed in the text.

given by $p = \text{erfc}(|r| \sqrt{N/2})$, where N is the number of data points [Press *et al.*, 2001]. Low values of p therefore indicate significance in the correlations. Only a subset of the data, delimited by the vertical dashed lines in Figure 9, were used in performing the correlation analyses. This interval corresponds to the main interval of continuous radar data coverage. At the start of the interval, FIR was located close to dusk and, as can be seen at \sim 0030 UT in Figure 9a, there appears to be a break in the radar backscatter and a discontinuity in its location. Prior to this time the backscatter moves equatorward at a slower rate than immediately afterwards such that the latter appears to project back in time to a much higher latitude than the former. Thus there appear to be two distinct equatorward moving patches, indicated in Figure 9a by the two horizontal bars. The earlier, lower

Table 1. Liner Pearson Correlation Coefficients (r) and the Corresponding Uncorrelated Probabilities (p) Between the SAID Latitude (Λ_S) and Velocity (vel_s) and Various Other Parameters From Figure 9^a

	Λ_S		vel_s	
	r	P	r	P
Λ_S	—	—	0.00	9.51×10^{-1}
vel_s	0.00	9.51×10^{-1}	—	—
var_s	0.50	8.00×10^{-15}	0.57	1.52×10^{-18}
$ H $	-0.34	1.88×10^{-7}	0.63	3.96×10^{-2}
$ Sym-H $	-0.50	1.46×10^{-14}	0.60	3.25×10^{-20}
$Asym-H$	-0.55	2.85×10^{-17}	0.57	1.54×10^{-18}
V_D	-0.12	5.86×10^{-2}	0.06	3.23×10^{-1}
V_D^*	-0.58	2.13×10^{-19}	0.40	9.71×10^{-10}

^a V_D^* corresponds to V_D with a 20 min time-lag imposed.

latitude patch might correspond to a latitudinally separated SAID that follows more closely the equatorward boundary of the auroral oval, merging with the one from higher latitudes. This could be related to observations discussed by *Anderson et al.* [2001], who noted that at dusk SAIDs are completely separated from the auroral zone, while near midnight they straddle its equatorward edge. At the other end of the interval, after ~ 0440 UT, the data were excluded simply because the radar backscatter becomes extremely patchy. This could be a result of a change in the nature of the electrodynamics associated with a change in interplanetary conditions, or simply related to the advancing local time of the radar.

[31] Returning to the correlation results in Table 1, we first consider those pertaining to the velocity of the SAID. $|H|$, Sym-H, and Asym-H all exhibit a significant level of correlation with vel_S , suggesting a relationship with substorm and ring current activity. This seems reasonable, considering that it is an injection of particles into the ring current following substorm onset that are understood to be responsible for the polarization electric fields that give rise to the SAID. However, the magnitude of the Sym-H perturbations are quite small (± 15 nT) and according to *Weygand and McPherron* [2006], the Asym-H index should better represent variations associated with substorm injections and consequent enhancements of the partial ring current. A comparison of the Sym-H and Asym-H indices does suggest that the modest enhancements apparent in Sym-H magnitude correspond to significant increases in asymmetry. This implies that it is the level of ring current asymmetry and associated substorm activity, rather than the ring current's overall strength, that are influencing the dynamics of the subauroral flows. It could also explain the existence of significant subauroral flows during intervals of low Sym-H magnitude, such as those discussed by *Oksavik et al.* [2006], during which Sym-H was only ± 10 nT while Asym-H peaked at ~ 80 nT. The significant correlation of $|H|$ with vel_S is also consistent with a discussion by *Makarevich and Dyson* [2007], who suggested that SAPS were a two-stage process, with an initial velocity increase associated with the establishment of the polarization electric field near to a substorm onset, followed by a more gradual evolution of the flows dependent on ongoing magnetosphere-ionosphere coupling processes.

[32] Next, we consider the possible control of the latitude of the SAID, Λ_S . The correlation coefficients in Table 1 reveal no obvious candidate, however, previous studies have suggested a relationship between the latitude of the SAPS and Sym-H (or D_{ST}), so we consider this here. In an analysis of the SAPS region during four severe storms ($D_{ST} < -200$ nT), *Huang and Foster* [2007] identified a linear relationship between D_{ST} and SAPS latitude using low-altitude spacecraft data. Subsequent statistical studies using low-altitude spacecraft [*Wang et al.*, 2008] and ionospheric radar data [*Kataoka et al.*, 2009] extended the range of D_{ST} to include much weaker ring current intervals and indicate an exponential relationship. For the interval of Sym-H; ~ 70 nT discussed in the present paper, the flows we observe with a magnetic latitude of $\sim 56^\circ$ - 58° are fully consistent with their findings. It is interesting to note, however, that the results of *Wang et al.* [2008] and *Kataoka et al.* [2009] imply that subauroral flows of over 1 km s^{-1}

can occur even when the ring current intensity is very low ($D_{ST} \sim 0$ nT), resulting in the latitude of the subauroral region reaching up to $\sim 70^\circ$. This supports our earlier suggestion that the strength of the ring current is unlikely to be a key factor in determining SAID dynamics. While it might be associated with the average latitude of a SAID simply as a result of the large-scale dependence of the auroral oval latitude on the ring current strength [*Milan et al.*, 2009], it seems more likely that the shorter-timescale dynamics of SAID will be governed by small-scale variations in Sym-H associated with enhancements in Asym-H related to substorm activity.

[33] Another candidate for controlling the latitude of the SAID is simply the level of solar wind – magnetosphere coupling. Unfortunately, having no global information regarding the size of the polar cap it is not possible to make an estimate of the related variation in total open flux content and hence the expected motion of the auroral oval. Nevertheless, by integrating V_D over the interval we can make an estimate of the change in open flux that would be expected if no nightside reconnection was taking place. This is shown in Figure 9f as ΔF (blue/dashed curve). According to *Milan et al.* [2010], the average auroral oval for $K_p = 6$ (appropriate for the start of our interval) has an equatorward boundary in the pre-midnight sector located at $\sim 56^\circ$, consistent with our observations. The associated poleward boundary is located at $\sim 71^\circ$ which, if taken as a proxy for the open-closed field line boundary, corresponds to a polar cap containing 0.72 GWb of open flux. The addition of a further 1.5 GWb of open flux over the duration of the interval would place the open-closed field line boundary at an unrealistically low latitude of $\sim 56^\circ$. This in turn would place the expected location of the equatorward boundary at a far lower latitude than it was observed. It is reasonable to conclude, therefore, that substantial tail reconnection occurs over the course of the interval. This would also be consistent with the correlation evident between Λ_S and the variability of the SAID velocity, var_S ($r = 0.50$). If the times when the SAID was retreating to higher latitudes corresponded to intervals of substorm activity and tail reconnection, then it might be expected that these times would exhibit small-scale variability in the flows typical of such intervals. Overall there is strong evidence to suggest that the latitudinal motion of the SAID, and of the equatorward boundary of the auroral oval, is a response to a motion of the poleward boundary due to large-scale solar wind – magnetosphere coupling. This can be inferred directly if V_D is shifted to later times by 20 min (corresponding to V_D^* in Table 1). In this case the correlation with Λ_S becomes significantly higher ($r = -0.58$). A delayed response to changes in the solar wind is also consistent with internal magnetospheric processes playing a role. *Clauer and McPherron* [1980], for example, found the onset of partial ring current disturbances to be consistently preceded by enhancements in the solar wind electric field with a delay of typically a few tens of minutes. In this way, the variations in V_D could also be responsible for the small-scale variations in Sym-H and Asym-H (Figure 9d).

4.2. Ionospheric Propagation

[34] The FIR observations of ionospheric radar scatter discussed in section 4.1 above have revealed evidence for

Table 2. Results of a Cross Correlation Analysis Between Λ_{GS} and Sym-H Showing Selected Lag Times (t), Corresponding Correlation Coefficients (r) and Uncorrelated Probabilities (p), and Linear Regression Coefficients m and c (Discussed in the Text)

t (h)	r	p	m	c
0	0.936	0.0218	4.96	-247
6.8	0.999	0.0144	5.69	-290
14	0.983	0.0160	11.6	-566

subauroral electric fields that clearly respond to the effects of solar wind-magnetosphere coupling as well as the electrodynamics of the inner magnetosphere. From a diagnostic perspective it is worthwhile to briefly consider whether these observations can reveal anything additional about the ionospheric conditions under which such observations can be made. It is certainly likely that the activity related to the storm itself will affect the ionospheric composition, and may precondition it in such a way as to facilitate such radar observations. Ionospheric characteristics such as electron density, for example, which are directly affected by geomagnetic activity, are also directly related to radar propagation paths which determine from where backscatter can be received. However, while the existence of ionospheric scatter provides evidence of such favorable conditions, the absence of ionospheric scatter at all other times does not provide much in addition. It is perhaps significant that according to Kataoka *et al.* [2009] and Wang *et al.* [2008] D_{ST} values as low as just -20 nT should result in the magnetic latitude of the SAPS region moving to $\sim 60^\circ$ (inside the field-of-view of the FIR) yet no evidence for FIR observations of similar flows at such latitudes exist for such modest D_{ST} (or Sym-H) values. It is reasonable to suppose, therefore, that higher levels of activity are required in order for the ionosphere to present favorable conditions to the radar.

[35] One diagnostic technique that can be used to investigate ionospheric propagation in the absence of ionospheric scatter is the location of ground backscatter. Ground backscatter is observed when the ionospheric refractive index is high enough to cause the transmitted radio wave to be reflected from the ionosphere down to the ground. A higher refractive index results in a shorter path length and the observation of ground scatter at ranges closer to the radar [Milan *et al.*, 1997]. The ionospheric refractive index is related to the electron density which can become enhanced during storms owing to an expansion of the polar ionization enhancement—a so-called positive storm effect [Prols et al., 1991]. It may also be caused when plumes of storm enhanced density (SED) [Foster, 1993] spanning the dusk sector get drawn out by SAPS eroding the outer plasma-sphere and midlatitude ionosphere. When this happens, a deep ionospheric trough forms at the center of the SAPS channel, while at lower latitudes plasma transport within the SED plume enhances total electron content [Foster and Rideout, 2007]. In a number of their events Foster and Rideout [2007] show elevated total electron content close to, or just poleward of, the location magnetically conjugate to FIR. It is possible, therefore, that SED is playing an important role in determining the backscatter characteristics

of the radar. A thorough statistical survey of the FIR backscatter statistics is beyond the scope of the present paper, but we briefly consider below what the behavior of the FIR ground backscatter observed during this interval might reveal about the ionospheric conditions.

[36] The long interval of data presented in Figure 2 included observations of radar ground backscatter over several days during the geomagnetic storm under investigation. The black crosses on the radar data in Figure 2d indicate the equatorward extent of ground backscatter observed during each day (Λ_{GS}). The scatter was observed to move closer to the radar as the main phase of the storm intensified, and then to retreat from the radar during the storm recovery phase. This is indicative of the storm effects on electron density discussed above and it is feasible that only those conditions that existed at the time of the maximum disturbance during the storm were suitable for the observation of ionospheric scatter at appropriate subauroral latitudes. To investigate quantitatively the relationship between Λ_{GS} and storm intensity we have performed a cross correlation analysis of Λ_{GS} and Sym-H, the results of which are shown in Table 2. Correlation coefficients (r) and uncorrelated probabilities (p) are shown for lags $t = 0$ h, 6.4 h (maximum correlation) and 14 h. Also shown are the corresponding coefficients of linear regression, m and c , where $\text{Sym-H} = m|\Lambda_{GS}| + c$. The colored crosses on Figure 2d correspond to values of Sym-H derived from this relationship for the same lag times (blue = 0 h, red = 6.4 h, green = 14 h). Although the correlation at zero lag is high, and the significance limited by the small sample size, these results are also consistent with the existence of a considerable delay between changes in Sym-H and the corresponding motion of the radar ground backscatter. A zero lag would imply that relatively small decreases in Sym-H of ~ -40 nT were associated with the equatorward motion of the ground backscatter, and that the ionospheric electron density would have been even more elevated during the interval in which the SAID was observed (when no ground backscatter measurements were made). On the other hand, if the peak Sym-H decreases of ~ -80 nT were associated with the most equatorward observations of the ground backscatter (corresponding to a lag of 14 h) then the associated electron density enhancements would have to have outlived the peak Sym-H decreases by many hours. Clearly this relationship needs to be investigated further in the future as more radar data become available from a wider range of geomagnetic conditions.

5. Summary

[37] On 4 August 2010, during the peak magnetic disturbance of a geomagnetic storm, a high velocity ($> 1000 \text{ m s}^{-1}$) channel of ionospheric plasma flow located at $\sim 55^\circ\text{S}$ and lasting ~ 6.5 hours was observed in the pre-midnight sector by the newly deployed Falkland Islands SuperDARN HF radar. Coincident flow data from the DMSP satellites and the magnetically near-conjugate northern hemisphere Blackstone HF radar reveal that the SAID was embedded within the broader subauroral polarization streams (SAPS). The ability of the radars to make continuous, high-resolution measurements over many hours of universal time, simultaneously over a range of magnetic local times, has enabled a detailed inspection of the characteristics of the flow channel

to be performed. Comparison of the evolution of the flows with interplanetary and low-altitude spacecraft data and ground-based geomagnetic observations have elucidated the characteristics of the storm-time subauroral ionosphere and its relationship to large-scale magnetospheric dynamics. In particular:

[38] 1. The SAID location remained close to, or equatorward of, the auroral electron precipitation boundary while remaining generally poleward of the equatorward boundary of the ion precipitation, consistent with a generation mechanism in the ring current.

[39] 2. The dynamic nature of the SAID velocity, and the existence of small-scale velocity perturbations within the SAID structure, are consistent with it being driven by dynamic tail processes such as substorm activity but not necessarily in response to global enhancements in ring current strength.

[40] 3. The variation in latitude of the SAID in concert with the equatorward boundary of auroral oval on comparable timescales to changes in the dayside reconnection rate imply a direct relationship between the subauroral ionosphere and solar wind–magnetosphere coupling.

[41] These results are consistent with SAID electric fields being generated by localized charge separation in the partial ring current, but suggest that their location is more strongly governed by solar wind driving and associated large-scale magnetospheric dynamics.

[42] **Acknowledgments.** The ACE SWEPAM and MAG instrument teams, the ACE Science Centre, and Ruth Skoug of the Los Alamos National Laboratory provided and assisted with the ACE spacecraft data. The World Data Centre for Geomagnetism, Kyoto, provided the ground magnetic indices with individual magnetometer data sets provided by the British Antarctic Survey and the Japanese National Institute of Polar Research. The DMSP particle detectors were designed by Dave Hardy of AFRL, and data obtained from JHU/APL. We also gratefully acknowledge the Center for Space Sciences at the University of Texas at Dallas and the US Air Force for providing the DMSP thermal plasma data. AG and SEM were supported during this study by NERC grant NE/G019665/1 and MPF by NERC grant NE/G018707/1. These NERC grants also support the Falkland Islands radar hardware and operations. SEM, ML and TKY were also supported by STFC grant ST/H002480/1. JBB and Blackstone radar operations are supported by NSF grants AGS-0849031 and AGS-0946900.

[43] Masaki Fujimoto thanks the reviewers for their assistance in evaluating this paper.

References

- Akasofu, S.-I. (1964), The development of the auroral substorm, *Planet. Space Sci.*, **12**, 273–282.
- Anderson, P. C., R. A. Heelis, and W. B. Hanson (1991), The ionospheric signatures of rapid subauroral ion drifts, *J. Geophys. Res.*, **96**(A4), 5785–5792.
- Anderson, P. C., W. B. Hanson, R. A. Heelis, J. D. Craven, D. N. Baker, and L. A. Frank (1993), A proposed production-model of rapid subauroral ion drifts and their relationship to substorm evolution, *J. Geophys. Res.*, **98**(A4), 6069–6078.
- Anderson, P. C., D. L. Carpenter, K. Tsuruda, T. Mukai, and F. J. Rich (2001), Multisatellite observations of rapid subauroral ion drifts (SAID), *J. Geophys. Res.*, **106**(A12), 29,585–29,599.
- Baker, K. B., and S. Wing (1989), A new magnetic coordinate system for conjugate studies at high-latitudes, *J. Geophys. Res.*, **94**(A7), 9139–9143.
- Chisham, G., et al. (2007), A decade of the Super Dual Auroral Radar Network (SuperDARN): Scientific achievements, new techniques and future directions, *Surv. Geophys.*, **28**, 33–109, doi:10.1007/s10712-007-9017-8.
- Clauer, C. R., and R. L. McPherron (1980), The relative importance of the interplanetary electric field and magnetospheric substorms on partial ring current development, *J. Geophys. Res.*, **85**(A12), 6747–6759.
- Cowley, S. W. H. (2000), Magnetosphere-ionosphere interactions: A tutorial review, in *Magnetospheric Current Systems*, *Geophys. Monogr. Ser.*, vol. 118, edited by S. Ohtani, pp. 91–106, AGU, Washington, D. C.
- Davis, T. N., and M. Sugiura (1966), Auroral electrojet activity index *AE* and its universal time variations, *J. Geophys. Res.*, **71**(3), 785–801.
- Elphinstone, R., J. Murphree, and L. Cogger (1996), What is a global auroral substorm?, *Rev. Geophys.*, **34**(2), 169–232.
- Etemadi, A., S. W. H. Cowley, M. Lockwood, B. J. I. Bromage, D. M. Willis, and H. Luhr (1988), The dependence of high-latitude dayside ionospheric flows on the north south component of the IMF—A high time resolution correlation-analysis using EISCAT Polar and AMPTE UKS and IRM data, *Planet. Space Sci.*, **36**, 471–498.
- Foster, J. C. (1993), Storm time plasma transport at middle and high-latitudes, *J. Geophys. Res.*, **98**(A2), 1675–1689.
- Foster, J. C. (1995), Radar observations of magnetosphere-ionosphere coupling at mid and high-latitudes, *J. Geomagn. Geoelectr.*, **47**(8), 801–812.
- Foster, J. C., and W. J. Burke (2002), SAPS: A new characterization for sub-auroral electric fields, *Eos Trans. AGU*, **83**(36), 393–394.
- Foster, J. C., and W. Rideout (2007), Storm enhanced density: Magnetic conjugacy effects, *Ann. Geophys.*, **25**, 1791–1799.
- Freeman, M. P., D. J. Southwood, M. Lester, T. K. Yeoman, and G. D. Reeves (1992), Substorm-associated radar auroral surges, *J. Geophys. Res.*, **97**(A8), 12,173–12,185.
- Galperin, Y. I., V. N. Ponomarev, and A. G. Zosimova (1973), Direct measurements of ion drift velocity in the upper ionosphere during a magnetic storm. 2. Results of measurements during the November 3, 1967, magnetic storm, *Cosmic Res., Engl. Transl.*, **11**, 283–292.
- Greenwald, R. A., et al. (1995), DARN/SuperDARN: A global view of the dynamics of high-latitude convection, *Space Sci. Rev.*, **71**, 761–796, doi:10.1007/BF00751350.
- Grocott, A., S. W. H. Cowley, J. B. Sigwarth, J. F. Watermann, and T. K. Yeoman (2002), Excitation of twin-vortex flow in the nightside high-latitude ionosphere during an isolated substorm, *Ann. Geophys.*, **20**, 1577–1601.
- Grocott, A., M. Lester, M. L. Parkinson, T. K. Yeoman, P. L. Dyson, J. C. Devlin, and H. U. Frey (2006), Towards a synthesis of substorm electrodynamics: HF radar and auroral observations, *Ann. Geophys.*, **24**, 3365–3381.
- Grocott, A., J. A. Wild, S. E. Milan, and T. K. Yeoman (2009), Superposed epoch analysis of the ionospheric convection evolution during substorms: Onset latitude dependence, *Ann. Geophys.*, **27**, 591–600.
- Grocott, A., S. E. Milan, N. Sato, J. A. Wild, T. K. Yeoman, and A. S. Yukimatu (2010), Superposed epoch analysis of the ionospheric convection evolution during substorms: IMF *B_y* dependence, *J. Geophys. Res.*, **115**, A00106, doi:10.1029/2010JA015728.
- Hardy, D. A., L. K. Schmitt, M. S. Gussenhoven, F. J. Marshall, H. C. Yeh, T. L. Shumaker, A. Hube, and J. Pantazis (1994), Precipitating electron and ion detectors (SSJ/4) for the block 5D/flights 6–10 DMSP satellites: Calibration and data presentation, *Tech. Rep. AFGL-TR-84-0317*, Air Force Geophys. Lab., Hanscom Air Force Base, Mass.
- Huang, C.-S., and J. C. Foster (2007), Correlation of the subauroral polarization streams (SAPS) with the Dst index during severe magnetic storms, *J. Geophys. Res.*, **112**, A11302, doi:10.1029/2007JA012584.
- Iyemori, T., and D. R. K. Rao (1996), Decay of the Dst field of geomagnetic disturbance after substorm onset and its implication to storm-substorm relation, *Ann. Geophys.*, **14**, 608–618.
- Karlsson, T., G. T. Marklund, L. G. Blomberg, and A. Malkki (1998), Subauroral electric fields observed by the Freja satellite: A statistical study, *J. Geophys. Res.*, **103**(A3), 4327–4341.
- Kataoka, R., K. Hosokawa, N. Nishitani, and Y. Miyoshi (2009), SuperDARN Hokkaido radar observation of westward flow enhancement in subauroral latitudes, *Ann. Geophys.*, **27**, 1695–1699.
- Khan, H., and S. W. H. Cowley (1999), Observations of the response time of high-latitude ionospheric convection to variations in the interplanetary magnetic field using EISCAT and IMP-8 data, *Ann. Geophys.*, **17**, 1306–1335, doi:10.1007/s005850050858.
- Kirkwood, S., H. J. Opgenoorth, and J. S. Murphree (1988), Ionospheric conductivities, electric-fields and currents associated with auroral substorms measured by the EISCAT radar, *Planet. Space Sci.*, **36**, 1359–1380.
- Koustov, A. V., R. A. Drayton, R. A. Makarevich, K. A. McWilliams, J.-P. St-Maurice, T. Kikuchi, and H. U. Frey (2006), Observations of high-velocity SAPS-like flows with the King Salmon SuperDARN radar, *Ann. Geophys.*, **24**, 1591–1608.
- Koustov, A., N. Nishitani, Y. Ebihara, T. Kikuchi, M. R. Hairston, and D. Andre (2008), Subauroral polarization streams: Observations with the Hokkaido and King Salmon SuperDARN radars and modeling, *Ann. Geophys.*, **26**, 3317–3327.

- Lui, A. T. Y. (1996), Current disruption in the Earth's magnetosphere: Observations and models, *J. Geophys. Res.*, *101*(A6), 13,067–13,088, doi:10.1029/96JA00079.
- Makarevich, R. A., and P. L. Dyson (2007), Dual HF radar study of the subauroral polarization stream, *Ann. Geophys.*, *25*, 2579–2591.
- Makarevich, R. A., A. C. Kellerman, Y. V. Bogdanova, and A. V. Koustov (2009), Time evolution of the subauroral electric fields: A case study during a sequence of two substorms, *J. Geophys. Res.*, *114*, A04312, doi:10.1029/2008JA013944.
- Maynard, N. C. (1978), On large poleward-directed electric fields at subauroral latitudes, *Geophys. Res. Lett.*, *5*(7), 617–618.
- Maynard, N. C., T. L. Aggson, and J. P. Heppner (1980), Magnetospheric observation of large sub-auroral electric-fields, *Geophys. Res. Lett.*, *7*(11), 881–884.
- McComas, D. J., S. J. Bame, P. Barker, W. C. Feldman, J. L. Phillips, P. Riley, and J. W. Griffee (1998), Solar Wind Electron Proton Alpha Monitor (SWEPAM) for the Advanced Composition Explorer, *Space Sci. Rev.*, *86*, 563–612, doi:10.1023/A:1005040232597.
- Milan, S. E., T. K. Yeoman, M. Lester, E. C. Thomas, and T. B. Jones (1997), Initial backscatter occurrence statistics from the CUTLASS HF radars, *Ann. Geophys.*, *15*, 703–718.
- Milan, S. E., J. A. Davies, and M. Lester (1999), Coherent HF radar backscatter characteristics associated with auroral forms identified by incoherent radar techniques: A comparison of CUTLASS and EISCAT observations, *J. Geophys. Res.*, *104*(A10), 22,591–22,604.
- Milan, S. E., G. Provan, and B. Hubert (2007), Magnetic flux transport in the Dungey cycle: A survey of dayside and nightside reconnection rates, *J. Geophys. Res.*, *112*, A01209, doi:10.1029/2006JA011642.
- Milan, S. E., J. Hutchinson, P. D. Boakes, and B. Hubert (2009), Influences on the radius of the auroral oval, *Ann. Geophys.*, *27*, 2913–2924.
- Milan, S. E., T. A. Evans, and B. Hubert (2010), Average auroral configuration parameterized by geomagnetic activity and solar wind conditions, *Ann. Geophys.*, *28*, 1003–1012.
- Morelli, J. P., et al. (1995), Radar observations of auroral zone flows during a multiple-onset substorm, *Ann. Geophys.*, *13*, 1144–1163.
- Oksavik, K., R. A. Greenwald, J. M. Ruohoniemi, M. R. Hairston, L. J. Paxton, J. B. H. Baker, J. W. Gjerloev, and R. J. Barnes (2006), First observations of the temporal/spatial variation of the sub-auroral polarization stream from the SuperDARN Wallops HF radar, *Geophys. Res. Lett.*, *33*, L12104, doi:10.1029/2006GL026256.
- Parkinson, M. L., M. Pinnock, H. Ye, M. R. Hairston, J. C. Devlin, P. L. Dyson, R. J. Morris, and P. Ponomarenko (2003), On the lifetime and extent of an auroral westward flow channel (AWFC) observed during a magnetospheric substorm, *Ann. Geophys.*, *21*, 893–913.
- Press, W. H., S. A. Teukelosky, W. T. Vetterling, and B. P. Flannery (2001), *Numerical Recipes: The Art of Scientific Computing*, 3rd ed., Cambridge Univ. Press, Cambridge, U. K.
- Prolss, G. W., L. H. Brace, H. G. Mayr, G. R. Carignan, T. L. Killeen, and J. A. Klobuchar (1991), Ionospheric storm effects at subauroral latitudes: A case-study, *J. Geophys. Res.*, *96*(A2), 1275–1288.
- Provan, G., M. Lester, A. Grocott, and S. W. H. Cowley (2005), Pulsed flows observed during an interval of prolonged northward IMF, *Ann. Geophys.*, *23*, 1207–1225.
- Rich, F. J., W. J. Burke, M. C. Kelley, and M. Smiddy (1980), Observations of field-aligned currents in association with strong convection electric-fields at sub-auroral latitudes, *J. Geophys. Res.*, *85*(A5), 2335–2340.
- Ruohoniemi, J. M., R. A. Greenwald, O. de la Beaujardière, and M. Lester (1993), The response of the high-latitude dayside ionosphere to an abrupt northward transition in the IMF, *Ann. Geophys.*, *11*, 544–555.
- Smiddy, M., M. C. Kelley, W. Burke, F. Rich, R. Sagalyn, B. Shuman, R. Hays, and S. Lai (1977), Intense poleward-directed electric-fields near ionospheric projection of plasmapause, *Geophys. Res. Lett.*, *4*(11), 543–546.
- Smith, C. W., J. L'Heureux, N. F. Ness, M. H. Acuña, L. F. Burlaga, and J. Scheifele (1998), The ACE magnetic fields experiment, *Space Sci. Rev.*, *86*, 613–632, doi:10.1023/A:1005092216668.
- Spiro, R. W., R. A. Heelis, and W. B. Hanson (1979), Rapid sub-auroral ion drifts observed by Atmosphere Explorer-C, *Geophys. Res. Lett.*, *6*(8), 657–660.
- Stone, E. C., A. M. Frandsen, R. A. Mewaldt, E. R. Christian, D. Margolies, J. F. Ormes, and F. Snow (1998), The Advanced Composition Explorer, *Space Sci. Rev.*, *86*, 1–22, doi:10.1023/A:1005082526237.
- Sugiura, M. (1964), Hourly values of equatorial Dst for IGY, *Ann. Int. Geophys. Year*, *35*, 945–948.
- Todd, H., S. W. H. Cowley, M. Lockwood, D. M. Wills, and H. Luhr (1988), Response-time of the high-latitude dayside ionosphere to sudden changes in the north-south component of the IMF, *Planet. Space Sci.*, *36*, 1415–1428.
- Wang, H., A. J. Ridley, H. Luehr, M. W. Liemohn, and S. Y. Ma (2008), Statistical study of the subauroral polarization stream: Its dependence on the cross-polar cap potential and subauroral conductance, *J. Geophys. Res.*, *113*, A12311, doi:10.1029/2008JA013529.
- Wanliss, J. A., and K. M. Showalter (2006), High-resolution global storm index: Dst versus SYM-H, *J. Geophys. Res.*, *111*, A02202, doi:10.1029/2005JA011034.
- Weygand, J. M., and R. L. McPherron (2006), Dependence of ring current asymmetry on storm phase, *J. Geophys. Res.*, *111*, A11221, doi:10.1029/2006JA011808.
- Yeoman, T. K., J. A. Davies, N. M. Wade, G. Provan, and S. E. Milan (2000), Combined CUTLASS, EISCAT and ESR observations of ionospheric plasma flows at the onset of an isolated substorm, *Ann. Geophys.*, *18*, 1073–1087.
- Zou, S., L. R. Lyons, M. J. Nicolls, C. J. Heinzelman, and S. B. Mende (2009a), Nightside ionospheric electrodynamics associated with substorms: PFISR and THEMIS ASI observations, *J. Geophys. Res.*, *114*, A12301, doi:10.1029/2009JA014259.
- Zou, S., L. R. Lyons, C. P. Wang, A. Boudouridis, J. M. Ruohoniemi, P. C. Anderson, P. L. Dyson, and J. C. Devlin (2009b), On the coupling between the Harang reversal evolution and substorm dynamics: A synthesis of SuperDARN, DMSP, and IMAGE observations, *J. Geophys. Res.*, *114*, A01205, doi:10.1029/2008JA013449.
-
- J. B. H. Baker, Bradley Department of Electrical and Computer Engineering, Virginia Polytechnic Institute and State University, Blacksburg, VA 24061, USA.
- M. P. Freeman, British Antarctic Survey, Natural Environment Research Council, High Cross, Madingley Road, Cambridge CB3 0ET, UK.
- A. Grocott, M. Lester, S. E. Milan, and T. K. Yeoman, Department of Physics and Astronomy, University of Leicester, University Road, Leicester LE1 7RH, UK. (a.grocott@ion.le.ac.uk)